Numerical Investigation of Transpiration Cooling Effects on Turbulent Boundary Layers

W. Dahmen⋆*, V. König*⋆†*, S. Müller*⋆ *and M. Rom*⋆
⋆*Institut für Geometrie und Praktische Mathematik, RWTH Aachen University*
Templergraben 55, 52056 Aachen, Germany
{dahmen, koenig, mueller, rom}@igpm.rwth-aachen.de
†Corresponding author

Abstract

Transpiration cooling as an active cooling technique is an innovative concept for reducing the high thermal loads of rocket thrust chambers. A coolant is driven through a porous material by a pressure difference between the coolant reservoir and the hot gas flow.

The present study numerically investigates the influence of the cooling gas injection on the temperature, the velocity and the local skin friction in the boundary layer of a subsonic turbulent hot gas channel flow. Here, the hot gas in the channel flows over a cooled porous ceramic matrix composite (CMC) material. Separate solvers are used for the hot gas flow and the porous medium flow, respectively. These are applied alternately and coupled to each other by boundary conditions imposed at the interface. The simulation results are compared with experimental data to validate the two solvers as well as the coupling and to provide complementary insight into the effects of the cooling which cannot be assessed from experimental measurements.

1. Introduction

Transpiration cooling is a promising concept for the reduction of thermal loads at walls in future space transportation systems. It is based on the injection of a coolant into a boundary layer through a porous material. The injection is driven by the pressure difference between the hot gas flow and the coolant reservoir. The hot gas in the boundary layer is displaced and a protective layer with lower temperature is formed on the surface of the cooled structure. An accompanying effect is the significant reduction of the resulting wall heat flux and the skin friction [1].

Compared with other active cooling techniques such as film or effusion cooling, transpiration cooling might offer advantages regarding the formation of stable films, see Linn & Kloker [2, 3] and Linn et al. [4], and the cooling efficiency. Current research activities concern the investigation of porous materials, which must be capable of withstanding high thermal loads while providing a sufficient cooling, and the performance of different cooling gases. Appropriate materials were investigated by Selzer et al. [5]. Experiments with different coolants in a hypersonic wind tunnel were performed by Gülhan & Braun [6]. Langener [7] and Langener et al. [8] investigated transpiration cooling with CMC materials, in particular composite carbon/carbon (C/C) materials at sub- and supersonic speeds.

In this paper, we focus on the numerical simulation of transpiration cooling of a subsonic turbulent hot gas channel flow, where both the cooling gas and the gas in the channel are air. For this configuration, experimental results are available from Schweikert et al. [9]. The simulations are carried out using separate solvers for the hot gas flow and for the porous medium flow, respectively. These are directly coupled to each other by alternately exchanging data at the interface where the coolant enters the hot gas flow. Since we are only interested in steady state solutions, the coupling is realized in a weak sense, i.e., we use a two-domain approach: both solvers are applied alternately where in each iteration the respective solver is converged to a steady state with respect to the boundary conditions at the interface provided by the solution of the other solver. This process is continued until no further changes in both solutions occur. One of the main challenges of this approach is the development of appropriate boundary conditions for the coupling at the interface.

Concerning the turbulent hot gas channel flow, we use the adaptive parallel solver Quadflow [10] which solves the compressible Reynolds-averaged Navier-Stokes equations. The core ingredients of Quadflow are: (i) the flow solver concept based on a finite volume discretization [11], (ii) the grid adaptation concept based on wavelet techniques [12]

and (iii) the grid generator based on B-spline mappings [13]. A variety of turbulence models is available from which we choose Wilcox's two-equation k-ω model with a modification for mass injection [14].

The porous medium flow is modeled by the continuity equation, the Darcy-Forchheimer equation and two temperature equations for both fluid and solid material. This model is discretized by a finite element scheme using the deal.II library [15]. In the following, we will refer to the two solvers as the flow solver and the porous medium solver, respectively.

First results for the validation of the two solvers and, in particular, of the coupling are reported in [1, 16–18]. In addition to the two-dimensional simulations with air as cooling gas presented in this paper, these former works contain results of three-dimensional simulations and simulations with argon instead of air injection. In this work, we focus on the effect of the cooling gas injection on the boundary layer of the hot gas flow. The comparisons with experimental data from Schweikert et al. [9] include boundary profiles for the temperature and the velocity in flow direction as well as the local skin friction reduction induced by the injection.

The present paper is structured as follows: The governing equations for modeling the turbulent hot gas channel flow and the porous medium flow as well as suitable boundary conditions are discussed in Sects. 2 and 3, respectively. In Sect. 4, the numerical methods for solving the coupled problem are described, addressing the discretizations for both solvers and the coupling strategy. Numerical results for a coupled two-dimensional simulation are presented and compared with experimental data in Sect. 5. A summary of the main results and an outlook on future work in Sect. 6 conclude the paper.

2. Physical Modeling: Hot Gas Flow

The turbulent hot gas channel flow can be described by the compressible Reynolds-averaged Navier-Stokes equations composed of equations representing the conservation of mass, momentum and total energy. These have to be complemented by a turbulence model.

2.1 Governing Equations

The Reynolds-averaged Navier-Stokes equations (RANS) are obtained by applying the Reynolds averaging

$$f(t,\mathbf{x}) = \bar{f}(t,\mathbf{x}) + f'(t,\mathbf{x}) \qquad \text{with} \qquad \bar{f}(t,\mathbf{x}) := \lim_{\Delta\to\infty} \frac{1}{\Delta}\int_t^{t+\Delta} f(\tau,\mathbf{x})d\tau \tag{1}$$

to each flow quantity f of the Navier-Stokes equations. In the compressible case, the resulting equations have a rather complex form due to fluctuations in the density ρ. Hence, the density averaging

$$f = \tilde{f} + f'' \qquad \text{with} \qquad \tilde{f} := \frac{\overline{\rho f}}{\bar{\rho}}\,, \tag{2}$$

which is called Favre averaging, is applied additionally. The turbulence quantities are modeled by Wilcox's two-equation k-ω model in its latest formulation [14], leading to two additional equations for the turbulence kinetic energy $\tilde{k}$ and the turbulent dissipation $\tilde{\omega}$, respectively. Both are mass-specific values and Favre-averaged. Overall, the set of equations in dimensional form using the Einstein summation convention reads

$$\frac{\partial\bar{\rho}}{\partial t} + \frac{\partial(\bar{\rho}\tilde{v}_j)}{\partial x_j} = 0\,, \tag{3}$$

$$\frac{\partial(\bar{\rho}\tilde{v}_i)}{\partial t} + \frac{\partial(\bar{\rho}\tilde{v}_i\tilde{v}_j)}{\partial x_j} = -\frac{\partial\bar{p}}{\partial x_i} + \frac{\partial}{\partial x_j}\left(\bar{\tau}_{ij} + \bar{\rho}\tilde{R}_{ij}\right), \tag{4}$$

$$\frac{\partial(\bar{\rho}\tilde{E})}{\partial t} + \frac{\partial(\tilde{v}_j(\bar{\rho}\tilde{E}+\bar{p}))}{\partial x_j} = \frac{\partial}{\partial x_j}\left(\tilde{v}_i\left(\bar{\tau}_{ij} + \bar{\rho}\tilde{R}_{ij}\right) - \left(\bar{q}_j + \bar{q}^t_j\right) + \overline{v''_i\tau_{ij}} - \frac{1}{2}\overline{\rho v''_i v''_i v''_j}\right), \tag{5}$$

$$\frac{\partial(\bar{\rho}\tilde{k})}{\partial t} + \frac{\partial(\bar{\rho}\tilde{v}_j\tilde{k})}{\partial x_j} = \bar{\rho}\tilde{R}_{ij}\frac{\partial\tilde{v}_i}{\partial x_j} - \beta^*\bar{\rho}\tilde{k}\tilde{\omega} + \frac{\partial}{\partial x_j}\left(\left(\mu + \sigma^*\frac{\bar{\rho}\tilde{k}}{\tilde{\omega}}\right)\frac{\partial\tilde{k}}{\partial x_j}\right), \tag{6}$$

$$\frac{\partial(\bar{\rho}\tilde{\omega})}{\partial t} + \frac{\partial(\bar{\rho}\tilde{v}_j\tilde{\omega})}{\partial x_j} = \alpha\frac{\tilde{\omega}}{\tilde{k}}\bar{\rho}\tilde{R}_{ij}\frac{\partial\tilde{v}_i}{\partial x_j} - \beta\bar{\rho}\tilde{\omega}^2 + \sigma_d\frac{\bar{\rho}}{\tilde{\omega}}\frac{\partial\tilde{k}}{\partial x_j}\frac{\partial\tilde{\omega}}{\partial x_j} + \frac{\partial}{\partial x_j}\left(\left(\mu + \sigma\frac{\bar{\rho}\tilde{k}}{\tilde{\omega}}\right)\frac{\partial\tilde{\omega}}{\partial x_j}\right). \tag{7}$$

This system is solved for the conservative flow quantities

$$\mathbf{U}_{NS} = \left(\bar{\rho}, \bar{\rho}\tilde{v}_1, \ldots, \bar{\rho}\tilde{v}_d, \bar{\rho}\tilde{E}, \bar{\rho}\tilde{k}, \bar{\rho}\tilde{\omega}\right), \tag{8}$$

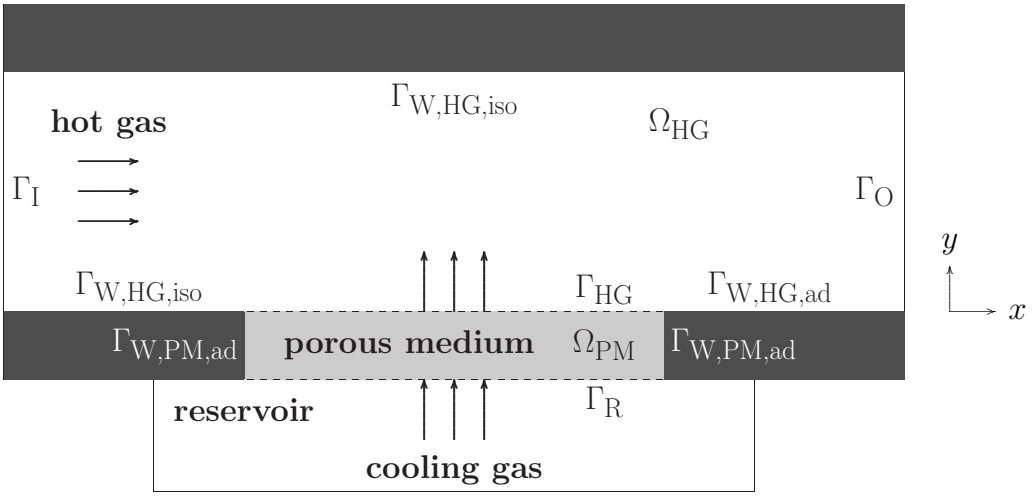

Figure 1: Configuration of coupled fluid-porous medium problem.

where $\tilde{\mathbf{v}} = (\tilde{v}_1, \ldots, \tilde{v}_d)^T$ is the fluid velocity vector and $\tilde{E}$ the total energy which is given by $\tilde{E} = \tilde{e} + 1/2\,\tilde{v}_i\tilde{v}_i$ with the specific internal energy $\tilde{e}$. The components of the mean viscous stress tensor $\bar{\tau}$ can be computed directly, whereas the Reynolds stress tensor $\bar{\rho}\tilde{R}$ is modeled via the Boussinesq hypothesis [19]. Fourier's law is applied to compute the mean heat flux $\bar{q}_j$, i.e.,

$$\bar{q}_j = -c_p \frac{\mu}{Pr} \frac{\partial \bar{T}}{\partial x_j}\,, \tag{9}$$

where c_p is the specific heat capacity at constant pressure, μ the dynamic viscosity, Pr the Prandtl number, which is set to 0.72 for air, and $\bar{T}$ the mean temperature. Analogously, the mean turbulent heat flux is approximated by

$$\bar{q}_j^t = -c_p \frac{\mu_t}{Pr_t} \frac{\partial \bar{T}}{\partial x_j} \tag{10}$$

with the turbulent Prandtl number set to $Pr_t = 0.9$. The turbulent viscosity μ_t is modeled by Wilcox's turbulence model, whereas the diffusion of the turbulent kinetic energy associated with $\partial/\partial x_j \left(\overline{v_i'' \tau_{ij}} - 1/2\,\overline{\rho v_i'' v_i'' v_j''}\right)$ in the energy equation (5) is neglected in eddy viscosity models. For the closure of the system, the equation of state for a thermally and calorically perfect gas

$$\bar{p} = \bar{\rho} R \tilde{T} \tag{11}$$

is used to relate the pressure to density and temperature. The specific gas constant R is evaluated by $R = (\gamma - 1)\, c_p/\gamma$ with the isentropic exponent γ, which is set to 1.4 for air. We refer to [14,20] for detailed information on the turbulence model and the choice of the coefficients $\beta^*, \sigma^*, \alpha, \beta, \sigma_d$ and σ.

In the following, we omit the labeling of averaged quantities ($\bar{\cdot}$ or $\tilde{\cdot}$) and denote the two-dimensional coordinate vector by $\mathbf{x} = (x, y)^T$ (see Fig. 1) and the velocity vector accordingly by $\mathbf{v} = (u, v)^T$.

2.2 Boundary Conditions and Initialization

The system (3) - (7) has to be complemented by suitable boundary conditions. A sketch of the complete coupled problem is depicted in Fig. 1. Here, we discuss the conditions for the subsonic hot gas flow. At the inflow boundary Γ_I, the velocity and the temperature are prescribed by

$$\mathbf{v} = \mathbf{v}_\infty, \quad T = T_\infty \qquad \text{on } \Gamma_I\,, \tag{12}$$

where the subscript ∞ indicates the inflow conditions. The static pressure on Γ_I is extrapolated from the interior flow domain.

At the outflow boundary Γ_O, only the pressure is prescribed by setting

$$p = p_\infty \qquad \text{on } \Gamma_O\,. \tag{13}$$

For the walls of the channel, we use isothermal ($\Gamma_{W,HG,iso}$) as well as adiabatic walls ($\Gamma_{W,HG,ad}$). The isothermal walls are needed to define cold walls (in relation to the adiabatic wall temperature) which occur in the experiment due

to the thermal behavior of the test section [9]. Downstream of the cooling gas injection, the cooled wall is modeled as an adiabatic wall to account for the changing wall temperature due to the cooling.

The coupling conditions at the interface Γ_{HG} include data from the porous medium flow: the velocity $\mathbf{v}_{PM}$ and the coolant temperature $T_{f,PM}$ are used to compute the density, velocity and total energy on Γ_{HG} such that

$$\rho = \frac{p}{R\,T_{f,PM}}, \quad \mathbf{v} = \mathbf{v}_{PM}, \quad E = \frac{R}{\gamma - 1} T_{f,PM} + \frac{1}{2}\left|\mathbf{v}_{PM}\right|^2 \qquad \text{on } \Gamma_{HG}\,. \tag{14}$$

We briefly express these relations in the following by

$$c_{HG}\left(\mathbf{U}_{NS}\,; \mathbf{v}_{PM}, T_{f,PM}|_{\Gamma_{HG}}\right) = 0\,. \tag{15}$$

The Wilcox turbulence model is modified according to [14] to account for the mass injection into the hot gas flow by applying the boundary condition

$$\omega = \frac{\rho u_\tau^2}{\mu} \frac{25}{\frac{v_{PM}}{u_\tau}\left(1 + 5\,\frac{v_{PM}}{u_\tau}\right)} \qquad \text{on } \Gamma_{HG}\,. \tag{16}$$

Here, v_{PM} from the porous medium flow is the normal component of the injection velocity and $u_\tau = \sqrt{\tau_w/\rho}$ the friction velocity. Values from the hot gas flow are used for the density ρ, the dynamic viscosity μ and the wall shear stress τ_w.

All initial hot gas flow quantities can be computed from the inflow conditions. For this purpose, the density ρ_∞, the temperature T_∞, the Mach number M_∞, the turbulence intensity $Tu_\infty = \sqrt{2/3\,\tilde{k}_\infty}/u_\infty$ and the ratio of the turbulent dynamic viscosity to the laminar dynamic viscosity $(\mu_t/\mu)_\infty$ are prescribed.

3. Physical Modeling: Porous Medium Flow

The pressure-driven laminar flow through porous material is modeled by taking into account the fluid compressibility, the fluid velocity and the heat conduction in the fluid as well as in the solid. Turbulent flow behavior is not expected to occur since the pore Reynolds number Re_p for the test case investigated in this paper is much lower than the critical value $Re_p \approx 300$. See, for instance, [7] for information on the pore Reynolds number.

3.1 Governing Equations

The continuum model for the porous medium flow consists of the continuity equation, the Darcy-Forchheimer (momentum) equation and two heat equations. We are particularly interested in properly capturing transport as well as non-equilibrium temperature effects. In the following, the model is briefly summarized. A more detailed discussion can be found in [21] and references cited therein.

In contrast to pure fluids, the porosity φ of the porous material has to be accounted for in the continuum model. It is defined as the ratio of void space to the total volume of the medium. We assume that all the void space is connected. Averaging the fluid velocity over a volume V_f consisting only of fluid, the intrinsic average velocity $\mathbf{V}$ is obtained. This is related to the Darcy velocity $\mathbf{v}$, i.e., the average velocity with respect to a volume element V_m comprising both solid and fluid material, by the porosity as $\mathbf{v} = \varphi\mathbf{V}$.

The system of equations for modeling the porous medium flow reads

$$\varphi\frac{\partial \rho_f}{\partial t} + \nabla\cdot\left(\rho_f \mathbf{v}\right) = 0\,, \tag{17}$$

$$\rho_f\left(\frac{1}{\varphi}\frac{\partial \mathbf{v}}{\partial t} + \frac{1}{\varphi^2}\left(\mathbf{v}\cdot\nabla\right)\mathbf{v}\right) = -\nabla p - \mu_f \mathbf{K}_\mathbf{D}^{-1}\mathbf{v} - \rho_f \mathbf{K}_\mathbf{F}^{-1}|\mathbf{v}|\mathbf{v}, \tag{18}$$

$$(1-\varphi)\rho_s c_{p,s}\frac{\partial T_s}{\partial t} = (1-\varphi)\nabla\cdot\left(\boldsymbol{\kappa_s}\,\nabla T_s\right) + h\left(T_f - T_s\right), \tag{19}$$

$$\varphi\rho_f c_{p,f}\left(\frac{\partial T_f}{\partial t} + \frac{1}{\varphi}\mathbf{v}\cdot\nabla T_f\right) = \varphi\nabla\cdot\left(\kappa_f\,\nabla T_f\right) + h\left(T_s - T_f\right). \tag{20}$$

This system is solved for the variables

$$\mathbf{U}_{PM} = \left(\rho_f, \mathbf{v}, T_s, T_f\right) \tag{21}$$

which denote the fluid density, the Darcy velocity, the solid temperature and the fluid temperature, respectively.

In the momentum balance (18), quadratic drag is included. Here, μ_f denotes the dynamic viscosity of the fluid, $\mathbf{K_D}$ the permeability tensor of the medium and $\mathbf{K_F}$ the Forchheimer coefficient, which is also a tensor. In the simulations presented in this paper, the contribution of the nonlinear Forchheimer term is small.

Two heat equations, see (19) and (20), are needed since the temperatures T_s of the solid and T_f of the fluid are assumed to be in non-equilibrium. In (19), $\boldsymbol{\kappa_s}$ is the heat conduction tensor, ρ_s the constant density of the solid and $c_{p,s}$ the specific heat capacity of the solid, while (20) contains the heat conduction coefficient κ_f, which is equal in all directions and therefore a scalar and not a tensor, and the specific heat capacity of the fluid $c_{p,f}$. The exchange of heat between the fluid and the solid is accounted for by the heat transfer coefficient h to be determined by experiments.

The pressure p is determined by the equation of state for a thermally and calorically perfect gas, with the specific gas constant R given by

$$p = \rho_f R T_f \,. \tag{22}$$

3.2 Boundary Conditions and Initialization

As can be seen in Fig. 1, we have to consider the inflow boundary Γ_R, where the cooling gas enters the porous medium from the reservoir, the outflow boundary Γ_{HG} at the interface to the hot gas flow and the bordering adiabatic side walls $\Gamma_{W,PM,ad}$.

The first boundary condition for the inflow boundary Γ_R concerns the fluid density ρ_f which is computed by the ideal gas law (22), yielding

$$\rho_f = \frac{p_c}{R\,T_{f,R}} =: \rho_{f,R} \qquad \text{on } \Gamma_R \,, \tag{23}$$

where p_c is the constant reservoir pressure. The temperatures on Γ_R are determined by incorporating the respective reservoir conditions. More precisely, denoting by T_b the temperature of the solid on the backside of the porous material, we set

$$T_s = T_b \,, \quad T_f = T_{f,R} \qquad \text{on } \Gamma_R \,, \tag{24}$$

where the fluid reservoir temperature $T_{f,R}$ is determined by the heat flux balance

$$-(1-\varphi)\,(\boldsymbol{\kappa_s}\nabla T_s)\cdot\mathbf{n} = c_{p,f}\,\rho_{f,R}\,v_y\left(T_{f,R} - T_c\right) \qquad \text{on } \Gamma_R \,. \tag{25}$$

The component v_y of the Darcy velocity $\mathbf{v}$ is the component in flow direction of the cooling gas, i.e., normal to the inflow boundary. The normal vector $\mathbf{n}$ points into the porous medium domain. The coolant temperature T_c is measured at one position in the reservoir (and not at the backside of the porous material) and is therefore a constant in the simulation.

Concerning the outflow boundary Γ_{HG}, the velocity component normal to Γ_{HG} is computed from the coolant mass flux $\dot{m}_c$ measured in the experiment such that

$$v_y = \frac{\dot{m}_c}{\rho_{HG} A_c} =: v_{y,HG} \qquad \text{on } \Gamma_{HG} \,, \tag{26}$$

where A_c denotes the surface area of the porous material. The density ρ_{HG} on Γ_{HG} is defined by $\rho_{HG} := p_{HG}/(R\,T_f)$ with the hot gas pressure p_{HG} and the porous medium fluid temperature T_f. The influence of the hot gas flow is also accounted for by the boundary condition

$$(\boldsymbol{\kappa_s}\nabla T_s)\cdot\mathbf{n} = c_{p,f}\,\rho_f\,v_{y,HG}\,(T_{HG} - T_f) + \kappa_{HG}\nabla T_{HG}\cdot\mathbf{n} \qquad \text{on } \Gamma_{HG} \tag{27}$$

with the heat conduction coefficient κ_{HG} of the fluid in the hot gas flow and the hot gas temperature T_{HG}. The normal vector $\mathbf{n}$ points into the hot gas domain. The heat flux balance (27) follows the approach presented in [22].

The side walls corresponding to $\Gamma_{W,PM,ad}$ are set to be adiabatic, i.e.,

$$\nabla T_s \cdot \mathbf{n} = 0 \,, \quad \nabla T_f \cdot \mathbf{n} = 0 \qquad \text{on } \Gamma_{W,PM,ad} \,. \tag{28}$$

From a physical perspective, the normal component of $\mathbf{v}$ must vanish on $\Gamma_{W,PM,ad}$, i.e.,

$$\mathbf{v}\cdot\mathbf{n} = 0 \qquad \text{on } \Gamma_{W,PM,ad} \,, \tag{29}$$

whereas nontrivial tangential components have to be permitted since no viscous effects are taken into account in the momentum equation (18).

Finally, suitable values for an initial guess in the porous medium domain Ω_{PM} have to be chosen. The density $\rho_{f,0}$ is determined by linearly interpolating the reservoir density and the hot gas density normal to Γ_R and Γ_{HG}, leading to

$$\rho_{f,0} = \frac{p_c}{R\,T_c} + \frac{y - y_R}{y_{HG} - y_R}\left(\frac{p_{HG}}{R\,T_{HG}} - \frac{p_c}{R\,T_c}\right) \qquad \text{in } \Omega_{PM}\,. \tag{30}$$

The fluid velocity $\mathbf{v}_0$ for the porous medium is then computed from the coolant mass flux $\dot{m}_c$ measured in the experiment and the initial density distribution such that

$$v_{x,0} = 0\,, \quad v_{y,0} = \frac{\dot{m}_c}{\rho_{f,0} A_c} \qquad \text{in } \Omega_{PM}\,. \tag{31}$$

The backside temperature T_b and the coolant reservoir temperature T_c are used as initial guess for the temperatures such that

$$T_{s,0} = T_b\,, \quad T_{f,0} = T_c \qquad \text{in } \Omega_{PM}\,. \tag{32}$$

4. Numerical Methods for Solving the Coupled Problem

In the following, we briefly describe the procedure of finding solutions $\mathbf{U}_{NS}$ and $\mathbf{U}_{PM}$ in the two flow regimes. We first discuss the numerical methods applied in the flow solver and in the porous medium solver, respectively. Subsequently, the coupling of both flow regimes is detailed. Further information on these topics can be found in [1, 17].

4.1 Discretization: Hot Gas Flow

By introducing

$$\mathbf{L}_{NS}(\mathbf{U}_{NS}) := \begin{pmatrix} \frac{\partial(\bar{\rho}\tilde{v}_j)}{\partial x_j} \\ \frac{\partial(\bar{\rho}\tilde{v}_i\tilde{v}_j)}{\partial x_j} + \frac{\partial \bar{p}}{\partial x_i} - \frac{\partial}{\partial x_j}\left(\bar{\tau}_{ij} + \bar{\rho}\tilde{R}_{ij}\right) \\ \frac{\partial(\tilde{v}_j(\bar{\rho}\tilde{E}+\bar{p}))}{\partial x_j} - \frac{\partial}{\partial x_j}\left(\tilde{v}_i\left(\bar{\tau}_{ij} + \bar{\rho}\tilde{R}_{ij}\right) - \left(\bar{q}_j + \bar{q}^t_j\right)\right) \\ \frac{\partial(\bar{\rho}\tilde{v}_j\tilde{k})}{\partial x_j} - \bar{\rho}\tilde{R}_{ij}\frac{\partial \tilde{v}_i}{\partial x_j} + \beta^*\bar{\rho}\tilde{k}\tilde{\omega} - \frac{\partial}{\partial x_j}\left(\left(\mu + \sigma^*\frac{\bar{\rho}\tilde{k}}{\tilde{\omega}}\right)\frac{\partial \tilde{k}}{\partial x_j}\right) \\ \frac{\partial(\bar{\rho}\tilde{v}_j\tilde{\omega})}{\partial x_j} - \alpha\frac{\tilde{\omega}}{\tilde{k}}\bar{\rho}\tilde{R}_{ij}\frac{\partial \tilde{v}_i}{\partial x_j} + \beta\bar{\rho}\tilde{\omega}^2 - \sigma_d\frac{\bar{\rho}}{\tilde{\omega}}\frac{\partial \tilde{k}}{\partial x_j}\frac{\partial \tilde{\omega}}{\partial x_j} - \frac{\partial}{\partial x_j}\left(\left(\mu + \sigma\frac{\bar{\rho}\tilde{k}}{\tilde{\omega}}\right)\frac{\partial \tilde{\omega}}{\partial x_j}\right) \end{pmatrix} \tag{33}$$

and with $\mathbf{U}_{NS}$ defined by (8), we can rewrite the system of equations (3) - (7) as

$$\frac{\partial \mathbf{U}_{NS}}{\partial t} + \mathbf{L}_{NS}(\mathbf{U}_{NS}) = \mathbf{0}\,. \tag{34}$$

In our computations, we are interested in *steady state* solutions. Therefore, the time variable t is used as a relaxation parameter in a backward Euler time discretization. The discrete counterpart of (34) then reads

$$(\Delta t)^{-1}\mathbf{U}^{n+1}_{NS} + \mathbf{L}^h_{NS}(\mathbf{U}^{n+1}_{NS}) = (\Delta t)^{-1}\mathbf{U}^n_{NS}, \quad n = 0, 1, 2, \dots\,. \tag{35}$$

The flow solver Quadflow [10] solves (35) by using a cell-centered fully adaptive finite volume method on locally refined grids.

4.2 Weak Formulation and Discretization: Porous Medium Flow

Analogously to the case of the hot gas flow, we are interested in steady state solutions for the porous medium flow. The solver has been implemented as a finite element solver using the deal.II library [15]. Therefore, the system of equations (17) - (20) is rewritten in a weak formulation, i.e., the objective is to find $\mathbf{U}_{PM} = \left(\rho_f, \mathbf{v}, T_s, T_f\right) \in X$ with a suitable trial space $X := X_{\rho_f} \times X_{\mathbf{v}} \times X_{T_s} \times X_{T_f}$ such that for all test functions $\mathbf{\Theta}_{PM} = \left(\hat{\rho}_f, \hat{\mathbf{v}}, \hat{T}_s, \hat{T}_f\right) \in Y$ with a suitable test space $Y := Y_{\rho_f} \times Y_{\mathbf{v}} \times Y_{T_s} \times Y_{T_f}$ one has

$$a^{PM}(\mathbf{U}_{PM}, \mathbf{\Theta}_{PM}) = F(\mathbf{\Theta}_{PM})\,, \quad \forall\, \mathbf{\Theta}_{PM} \in Y\,. \tag{36}$$

The derivation of (36) can be found in [17]. Here, we present the final formulation. The bilinear form $a^{PM}(\mathbf{U}_{PM}, \mathbf{\Theta}_{PM})$ is composed of the bilinear forms for each of the four equations of the system, i.e.,

$$\begin{aligned} a^{PM}(\mathbf{U}_{PM}, \mathbf{\Theta}_{PM}) := a_{\rho_f}(\mathbf{U}_{PM}, \mathbf{\Theta}_{PM}) \quad &+ \quad a_{\mathbf{v}}(\mathbf{U}_{PM}, \mathbf{\Theta}_{PM}) \\ &+ \quad a_{T_s}(\mathbf{U}_{PM}, \mathbf{\Theta}_{PM}) + a_{T_f}(\mathbf{U}_{PM}, \mathbf{\Theta}_{PM}) \end{aligned} \tag{37}$$

where $a_{\rho_f}, a_{\mathbf{v}}, a_{T_s}$ and a_{T_f} (omitting the dependence on $\mathbf{U}_{PM}$ and $\mathbf{\Theta}_{PM}$) are given by

$$a_{\rho_f} := \int_\Omega \hat{\rho}_f \nabla \cdot (\rho_f \mathbf{v}) \,, \tag{38}$$

$$a_{\mathbf{v}} := \int_\Omega \hat{\mathbf{v}} \cdot \left(\frac{1}{\varphi^2} \rho_f (\mathbf{v} \cdot \nabla)\mathbf{v} + \nabla(\rho_f R\, T_f) + \mu \mathbf{K}_\mathbf{D}^{-1} \mathbf{v} + \mathbf{K}_\mathbf{F}^{-1} \rho_f |\mathbf{v}| \mathbf{v} \right) , \tag{39}$$

$$a_{T_s} := (1-\varphi) \left(\int_\Omega \nabla \hat{T}_s \cdot \boldsymbol{\kappa_s} \nabla T_s + \int_{\Gamma_{HG}} \hat{T}_s c_{p,f}\, \rho_f\, v_{y,HG}\, T_f \right) - h \int_\Omega \hat{T}_s (T_f - T_s) \,, \tag{40}$$

$$a_{T_f} := \int_\Omega \hat{T}_f \left(\rho_f c_{p,f} \mathbf{v} \cdot \nabla T_f + h(T_f - T_s) \right) + \varphi \kappa_f \left(\int_\Omega \nabla \hat{T}_f \cdot \nabla T_f - \int_{\Gamma_{HG}} \hat{T}_f \nabla T_f \cdot \mathbf{n} \right) . \tag{41}$$

The right-hand side functional in (36) is given by

$$F(\mathbf{\Theta}_{PM}) = (1-\varphi) \int_{\Gamma_{HG}} \hat{T}_s \left(c_{p,f}\, \rho_f\, v_{y,HG}\, T_{HG} + \kappa_{HG}\, \nabla T_{HG} \cdot \mathbf{n} \right) . \tag{42}$$

To be able to formulate proper coupling conditions between the hot gas and the porous medium flow, we shall write

$$F(\mathbf{\Theta}_{PM}) = F(\mathbf{\Theta}_{PM}; T_{HG}, \nabla T_{HG}) \tag{43}$$

to express the dependence of F in (36) on data that will eventually come from the hot gas flow in the channel.

The trial spaces are defined by

$$X_{\rho_f} := \left\{ \rho_f \in H^1(\Omega) \cap L_\infty(\Omega) : \rho_f|_{\Gamma_R} = \rho_{f,R} \right\} , \tag{44}$$

$$X_{\mathbf{v}} := \left\{ \mathbf{v} \in H^1(\Omega)^d \cap L_\infty(\Omega)^d : \mathbf{v}|_{\Gamma_{HG}} = \mathbf{v}_{HG} \right\} , \tag{45}$$

$$X_{T_s} := \left\{ T_s \in H^1(\Omega) : T_s|_{\Gamma_R} = T_b \right\} , \tag{46}$$

$$X_{T_f} := \left\{ T_f \in H^1(\Omega) : T_f|_{\Gamma_R} = T_{f,R} \right\} \tag{47}$$

and the test spaces by

$$Y_{\rho_f} := H^1_{0,\Gamma_R}(\Omega), \quad Y_{\mathbf{v}} := \left(H^1_{0,\Gamma_{HG}}(\Omega) \right)^d , \quad Y_{T_s} := H^1_{0,\Gamma_R}(\Omega), \quad Y_{T_f} := H^1_{0,\Gamma_R}(\Omega) \,. \tag{48}$$

To approximate the solution of (36), we choose a suitable finite element trial space $X_h \subset X$ and a corresponding test space $Y_h \subset Y$, incorporating the respective boundary constraints given in (44) - (47). The Dirichlet conditions (24) on Γ_R for the elliptic part (40), (41) are incorporated as essential boundary conditions in the trial spaces (46), (47) which are therefore affine and not linear. All boundary conditions for the hyperbolic part (38), (39) are natural ones enforced weakly through the right-hand side functional (42).

Since all component spaces are subspaces of H^1, we use multilinear finite elements for all spaces. One then has to solve

$$a^{PM}(\mathbf{U}^h_{PM}, \mathbf{\Theta}^h_{PM}) = F(\mathbf{\Theta}^h_{PM}) \,, \quad \mathbf{\Theta}^h_{PM} \in Y_h \,. \tag{49}$$

More specifically, denoting by $\{\mathbf{U}^i_{PM} : i = 1, \ldots, N_h\}$, $\{\mathbf{\Theta}^i_{PM} : i = 1, \ldots, N_h\}$ bases for X_h, Y_h, respectively, (49) amounts to finding for each of the physical quantities $\zeta \in \{\rho_f, v_1, \ldots, v_d, T_s, T_f\}$ the array $(u^\zeta_i : i = 1, \ldots, N_h)$ for which $(\mathbf{U}^h_{PM})_\zeta = \sum_{i=1}^{N_h} u^\zeta_i (\mathbf{U}^i_{PM})_\zeta$ satisfies

$$a^{PM}(\mathbf{U}^h_{PM}, \mathbf{\Theta}^i_{PM}) = F(\mathbf{\Theta}^i_{PM}) \,, \quad i = 1, \ldots, N_h \,, \tag{50}$$

which is a *nonlinear* system of equations of size N_h.

The first two components of (49) corresponding to (38) and (39) form a nonlinear hyperbolic system, whereas the last two components corresponding to (40) and (41) form a linear elliptic system. Hence, we employ operator splitting to solve (50), i.e., we split $\mathbf{U}^h_{PM}$ into the convective and diffusive components $\mathbf{U}^h_{PM} = [\mathbf{U}^h, \mathbf{T}^h]$ with $\mathbf{U}^h = (\rho_{f,h}, \mathbf{v}_h)$, $\mathbf{T}^h = (T_{s,h}, T_{f,h})$ and alternately solve the elliptic system

$$a_T([\mathbf{U}^{h,old}, \mathbf{T}^{h,new}], \mathbf{\Theta}^h_{PM}) = F(\mathbf{\Theta}^h_{PM}) + a_U(\mathbf{U}^{h,old}_{PM}, \mathbf{\Theta}^h_{PM}) \,, \quad \mathbf{\Theta}^h_{PM} \in Y_h \tag{51}$$

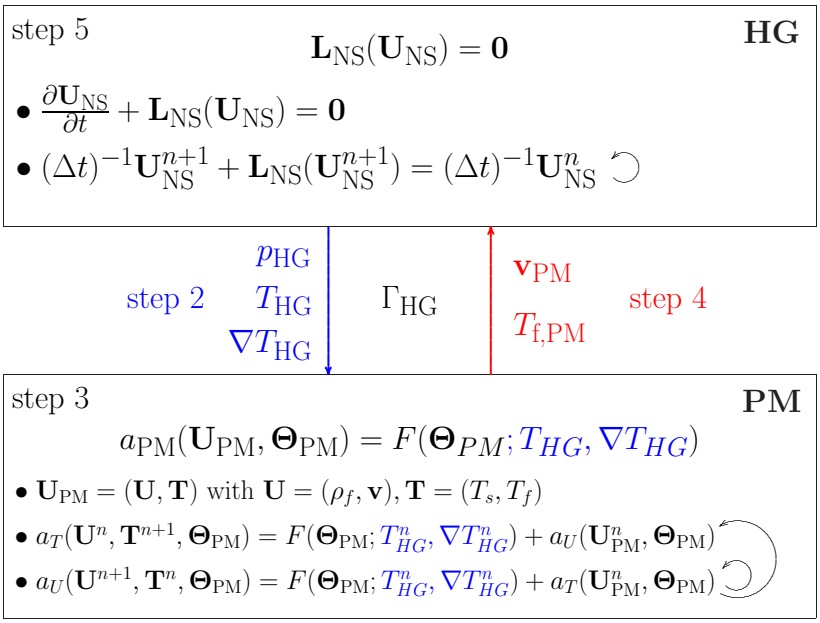

Figure 2: Illustration of the steps 2 to 5 of the iterative process for coupling hot gas and porous medium flow.

and the hyperbolic system

$$a_U([\mathbf{U}^{h,new}, \mathbf{T}^{h,old}], \mathbf{\Theta}_{PM}^h) = F(\mathbf{\Theta}_{PM}^h) + a_T(\mathbf{U}_{PM}^{h,old}, \mathbf{\Theta}_{PM}^h), \quad \mathbf{\Theta}_{PM}^h \in Y_h, \tag{52}$$

where $a_U = a_{\rho_f} + a_{\mathbf{v}}$ and $a_T = a_{T_s} + a_{T_f}$. The iteration is initialized by solving (51) first which we refer to as the *outer iteration* in the porous medium solver. Since the two temperature equations are linear, the linear system of equations evolving from the finite element discretization can be solved directly. The nonlinear hyperbolic part (52) is solved iteratively, which we call the *inner iteration*.

4.3 Coupling Both Flow Regimes

For the solution of the coupled problem, we alternately solve the systems

$$a^{PM}(\mathbf{U}_{PM}^{n+1}, \mathbf{\Theta}_{PM}) = F(\mathbf{\Theta}_{PM}; T_{HG}^n, \nabla T_{HG}^n) \quad \forall\, \mathbf{\Theta}_{PM} \in Y \tag{53}$$

and

$$\mathbf{L}_{NS}(\mathbf{U}_{NS}^{n+1}) = 0, \quad c_{HG}\left(\mathbf{U}_{NS}^{n+1}; \mathbf{v}_{PM}^n, T_{f,PM}^n\,|_{\Gamma_{HG}}\right) = 0 \tag{54}$$

approximately, employing the discretizations described before. In (53), the temperature T_{HG} and its gradient determine the right-hand side functional (42) in the porous medium system. Furthermore, p_{HG} enters to recompute the velocity which is then given by (26). In (54), the fluid temperature $T_{f,PM}$ and the velocity field $\mathbf{v}_{PM}$ from the porous medium, see (14), enter as data for the hot gas channel flow.

We continue with alternately solving the two systems until

$$\left\| q_1(\mathbf{U}_{NS}^{n+1})\,|_{\Gamma_{HG}} - q_1(\mathbf{U}_{NS}^{n})\,|_{\Gamma_{HG}} \right\|_\infty \le \varepsilon_1, \quad \left\| q_2(\mathbf{U}_{PM}^{n+1})\,|_{\Gamma_{HG}} - q_2(\mathbf{U}_{PM}^{n})\,|_{\Gamma_{HG}} \right\|_\infty \le \varepsilon_2 \tag{55}$$

for flow quantities $q_1 \in \{\rho, T\}$ and $q_2 \in \{v_y, T_f\}$ and given tolerances $\varepsilon_1 > 0$ and $\varepsilon_2 > 0$. By applying these conditions, we check the change of the flow quantities at the interface Γ_{HG} from one iteration to the next. If the maximal absolute difference between two iterations is small enough, the iterative process is stopped and the stationary *equilibrium solution* of the coupled system is obtained.

The iterative process can be summarized as given in the list below. The steps 2 to 5 of this process are illustrated in Fig. 2 together with additional information on the solution procedure in the respective solver.

Step 1: Initialize the flow solver.
Step 2: Transfer data $(p_{HG}, T_{HG}, \nabla T_{HG})$ provided by the flow solver to the porous medium solver.
Step 3: Converge the porous medium solver.
Step 4: Transfer data $(\mathbf{v}_{PM}, T_{f,PM})$ from the porous medium solver to the flow solver.

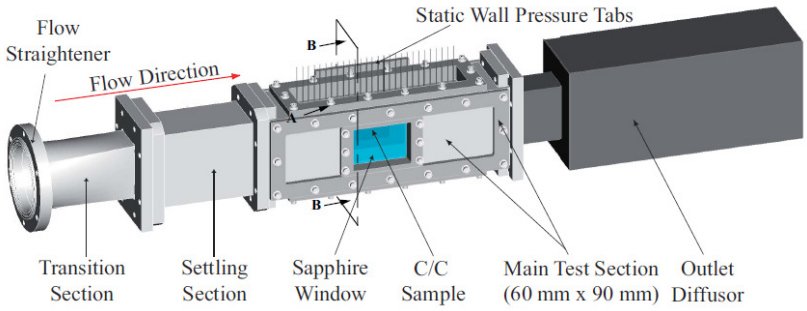

(a) Hot gas channel

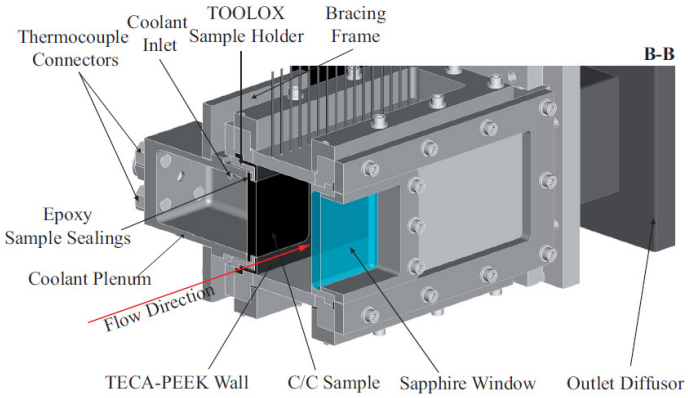

(b) Sample integration

Figure 3: Experimental setup by Langener et al. [8].

Step 5: Converge the flow solver.
Step 6: Perform grid adaptation in the flow solver.
Step 7: Stop if (55) is fulfilled or return to step 2.

5. Numerical Results

In this section, we study the behavior of the cooled boundary layer of a turbulent channel flow with respect to temperature, velocity and skin friction. For this purpose, we compare simulation results with experimental data. This is not only useful for the validation of our two solvers regarding the implementation, the boundary conditions and the coupling at the interface but also for gaining additional insight into the physical effects in the boundary layer. At first, the experimental setup for the turbulent channel flow and the characteristics of the porous material are briefly described, followed by the numerical setup and the simulation results.

5.1 Experimental Test Case

For the experiments, the porous material is mounted into the sidewall of a subsonic wind tunnel. On the backside of the porous material, a coolant reservoir is attached. The experimental setup is shown in Fig. 3. The test section is 1.32 m long with the porous material beginning 0.58 m downstream of the entrance, the height is 90 mm and the width 60 mm. The porous probe measures 61 mm $\times$ 61 mm and is 15 mm thick. Detailed information on the test facility can be found in [8]. The instrumentation for measuring pressure and temperature in the boundary layer is described in [9].

For the porous material, carbon/carbon (C/C) ceramics are used, produced by the DLR Stuttgart [5]. C/C material is a ceramic matrix composite (CMC) where both fibers and matrix are made from carbon. In the following, a single experimental configuration is investigated. In this case, the porous medium is mounted into the wall such that the flow through the material is parallel to one layer of the ceramic fibers.

The flow conditions in the hot gas channel and for the cooling gas are listed in Tabs. 1 and 2, respectively. Parameters of the porous material are given in Tab. 3. Note that the heat transfer coefficient h can only be estimated and not measured.

Table 1: Hot gas inflow conditions.

Mach number	M_∞	0.3
density	ρ_∞	$0.78\,kg/m^3$
temperature	T_∞	$425\,K$
pressure	p_∞	$95\,200\,Pa$

Table 2: Cooling conditions.

coolant mass flow rate	$\dot{m}_c$	$1.91\,g/s$
reservoir pressure	p_R	$334\,000\,Pa$
coolant reservoir temp.	T_c	$304.2\,K$
backside temperature	T_b	$321.9\,K$

Table 3: List of porous medium parameters.

throughflow direction		parallel
porosity	φ	0.111
effective heat conductivity	κ_s	$13.5\,W/(mK)$
permeability	K_D	$3.57 \cdot 10^{-13}\,m^2$
Forchheimer coefficient	K_F	$5.17 \cdot 10^{-8}\,m$
heat transfer coefficient	h	$10^6\,W/(m^2K)$

5.2 Numerical Setup

For the simulation of the test case described above, we choose $q_1 = \rho$ and $q_2 = v_y$ with the tolerances $\varepsilon_1 = 10^{-3}$ and $\varepsilon_2 = 10^{-4}$ to terminate the iterative coupling process according to (55). Here, these tolerances are reached after five coupling iterations.

The coarse grid for the flow solver comprises about 150 000 grid cells. The grid lines are concentrated towards the walls using a stretching function. The final adaptive grid after five coupling iterations and, hence, adaptations consists of about 480 000 grid cells, see Fig. 4(a).

The porous material is discretized by a coarse grid with 5×3 degrees of freedom which is then uniformly refined four times. After that, the respective first layer of cells at the interface to the hot gas side is repeatedly refined in x-direction until there are two interface cells for each cell in the hot gas. The grid lines are concentrated towards the hot gas and towards the reservoir side by applying a stretching technique. The upper left corner of the grid is depicted in Fig. 4(b).

Extensive information on the numerical setup, including a convergence study, can be found in [17].

5.3 Simulation Results

We first present the fluid temperature distribution in the porous medium and in the channel, before we discuss the influence of the cooling gas injection on the boundary layer of the channel flow.

Figure 5 shows the fluid temperature in the porous material. At the interface to the channel, the solid structure and, hence, the coolant is hotter at the leading edge of the porous medium and cooler downstream because of the developing cooling film in the channel. Due to the large heat transfer coefficient h causing a strong coupling of the solid temperature with the fluid temperature, the coolant quickly heats up downstream of the reservoir where it enters

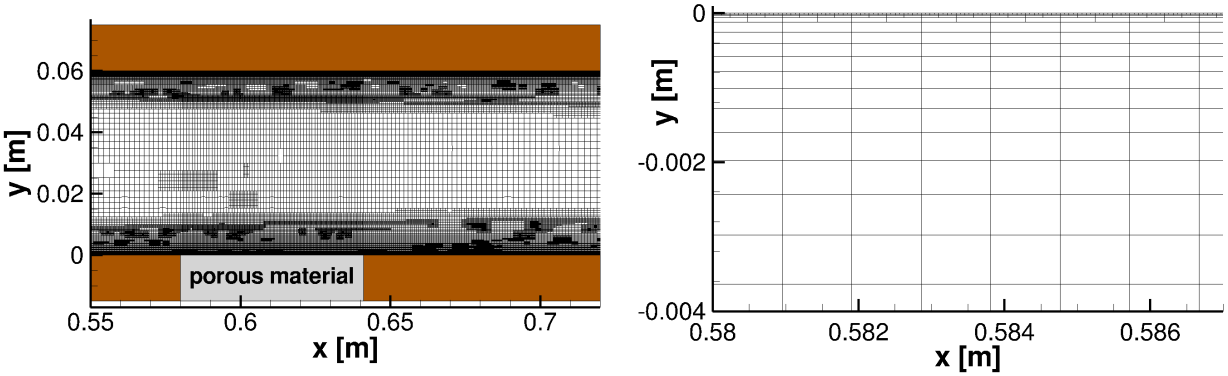

(a) Detail of adaptive grid for hot gas flow.

(b) Detail of grid for porous medium flow.

Figure 4: Details of final grids.

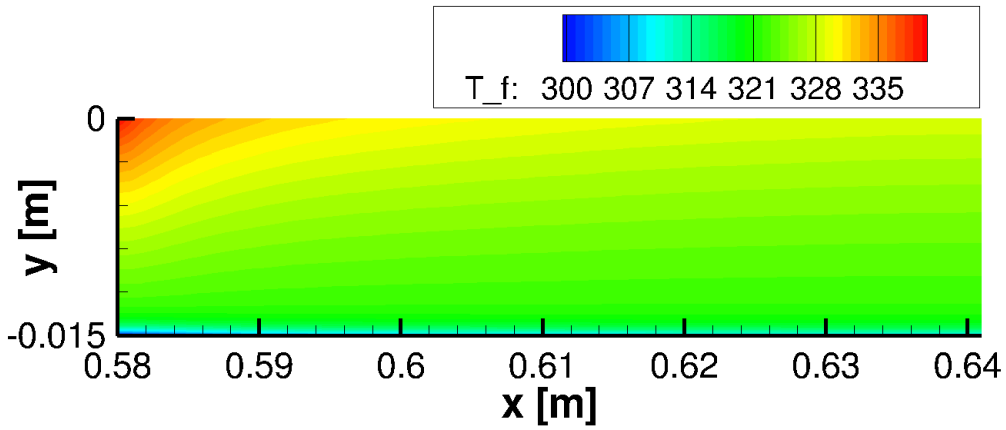

Figure 5: Fluid temperature in the porous material.

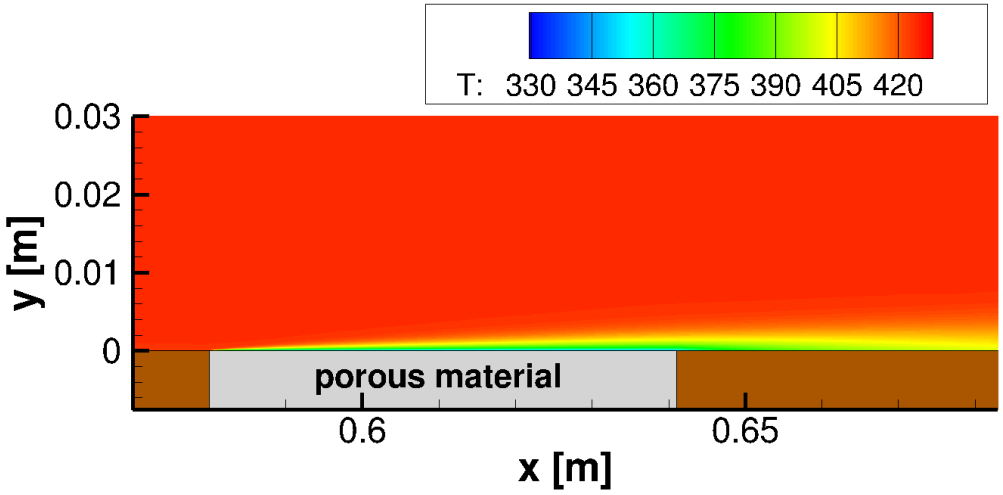

Figure 6: Temperature in the hot gas channel.

the porous medium. This effect corresponds to the experimental observations for the investigated porous material. The solid temperature exhibits essentially the same behavior as the fluid temperature which is also caused by the strong coupling. However, the temperatures are still in non-equilibrium.

The cooling film in the hot gas flow is depicted in Fig. 6. Its thickness increases over the length of the porous probe. Downstream of the trailing edge, the temperature in the coolant layer increases, mainly due to turbulent mixing.

Boundary profiles for the normalized temperature T/T_∞ over the normalized channel height y/H in the hot gas flow at two positions directly above the porous wall ($x = 0.6\,\mathrm{m}$ and $x = 0.63\,\mathrm{m}$) and one downstream of the injection ($x = 0.66\,\mathrm{m}$) are shown in Fig. 7, each one comparing simulation results with experimental data. In addition to the cooling test case, these plots include a test case for the same hot gas channel data without cooling gas injection. Especially for the two positions above the injection, the agreement of the simulation results with the experimental data is good. For $x = 0.66\,\mathrm{m}$ downstream of the injection, the values coincide for a height of $y/H > 0.032$. The lowest temperature in the experiment is measured at $y/H = 0.0083$ with a value of $T/T_\infty = 0.958$, whereas the simulation results in $T/T_\infty = 0.939$ at that height. Hence, the maximal temperature difference between the simulation and the experiment is 8.1 K, which corresponds to a deviation of about 2 %. The experimental data at that position ($x = 0.66\,\mathrm{m}$) indicate an adiabatic behavior. Even though the channel wall downstream of the porous medium is modeled as an adiabatic wall, cf. Fig. 1, the simulation does not reproduce the adiabatic temperature profile of the experiment. Only in a very thin region from $y/H = 0$ to $y/H \approx 0.002$, the simulation results show the typical adiabatic behavior. This discrepancy should be subject to further investigations.

The simulation confirms the observation of the experiment that the influence of the cooling gas injection ranges up to $y/H \approx 0.1$ at the position $x = 0.63\,\mathrm{m}$ [9]. Measuring flow quantities in the boundary layer is technically limited

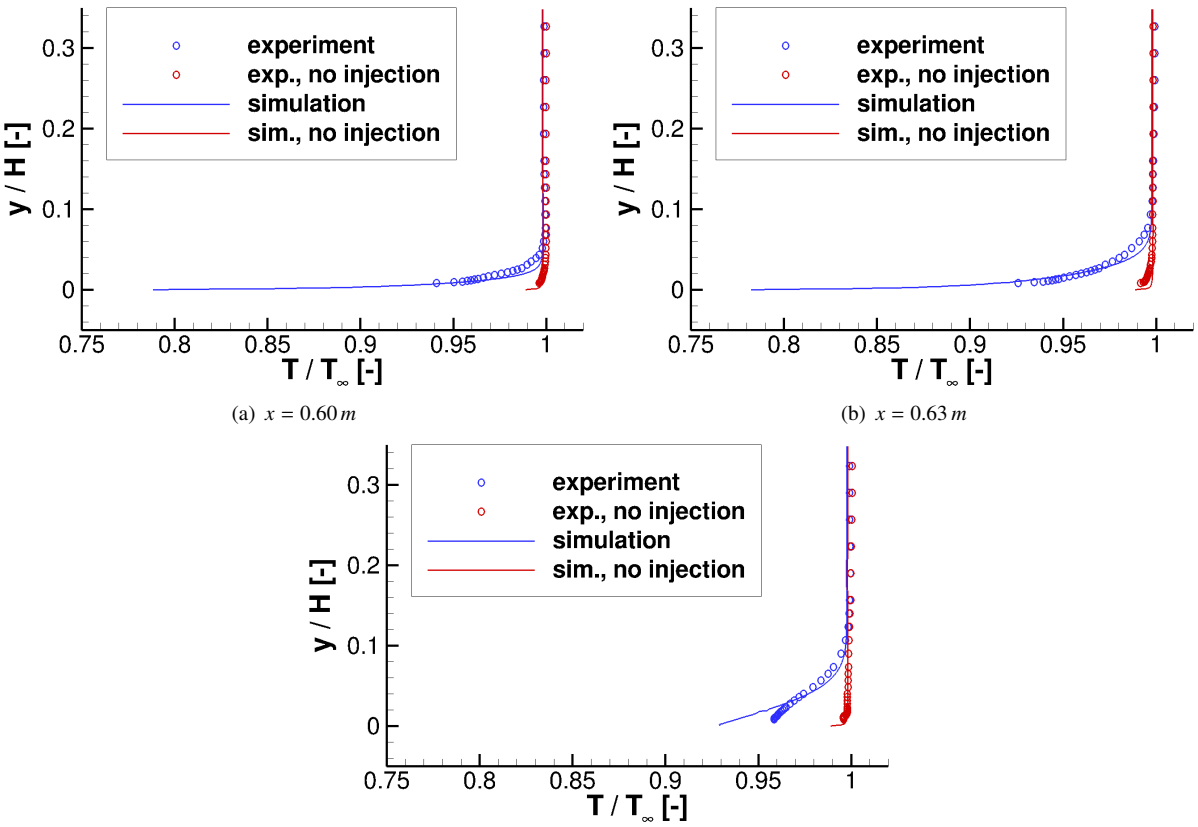

(a) $x = 0.60\,m$ (b) $x = 0.63\,m$

(c) $x = 0.66\,m$

Figure 7: Temperature boundary profiles for the hot gas channel flow.

regarding the coverage of the complete boundary layer. The lowest temperature in the experiment is approximately $T/T_\infty = 0.92$, whereas the temperatures decrease up to $T/T_\infty = 0.78$ close to the wall in the simulation. Here, the numerical simulation gives complementary insight into the cooling behavior in the channel that cannot be assessed from experimental measurements.

The velocity profiles in Fig. 8 show the normalized fluid velocity u/u_∞ in streamwise direction. Again, the agreement of simulation results with experimental data is good. The deceleration of the flow induced by the coolant injection can be clearly seen. The experiment confirms the influence of the injection ranging up to $y/H \approx 0.1$ at $x = 0.63$ m, whereas the velocities already agree at $y/H \approx 0.085$ in the case of the simulation.

Figure 9 presents semi-logarithmic plots of the dimensionless temperature T^+ and the dimensionless velocity u^+ in streamwise direction

$$T^+ = \frac{T_w - T}{T_\tau}, \quad u^+ = \frac{u}{u_\tau} \tag{56}$$

over the dimensionless wall distance

$$y^+ = \frac{\rho_w}{\mu_w} u_\tau y\,. \tag{57}$$

Here, the subscript w refers to wall conditions. The friction temperature T_τ is defined by $T_\tau = q_w/\left(\rho c_p u_\tau\right)$ and the friction velocity u_τ by $u_\tau = \sqrt{\tau_w/\rho_w}$ (cf. Sect. 2.2). The plots show a typical behavior for a turbulent channel flow at the position $x = 0.5$ m upstream of the injection, corresponding to the temperature profile proposed by Huang and Coleman [23]

$$T^+ = \begin{cases} Pr\,u^+ + \frac{1}{2}\frac{Pr}{c_p}\frac{u_\tau^2}{T_\tau}u^{+2} & \text{if } 0 \le y^+ \le 5 \quad \text{(viscous sublayer)} \\ Pr_t u^+ + \frac{1}{2}\frac{Pr_t}{c_p}\frac{u_\tau^2}{T_\tau}u^{+2} & \text{if } y^+ > 5 \quad \text{(logarithmic layer)} \end{cases} \tag{58}$$

and von Kármán's well-known velocity profile [24]

$$u^+ = \begin{cases} y^+ & \text{if } 0 \le y^+ \le 5 \quad \text{(viscous sublayer)} \\ 5\ln(y^+) - 3.05 & \text{if } 5 < y^+ \le 30 \quad \text{(buffer layer)} \\ 2.5\ln(y^+) + 5.5 & \text{if } y^+ > 30 \quad \text{(logarithmic layer)} \end{cases}. \tag{59}$$

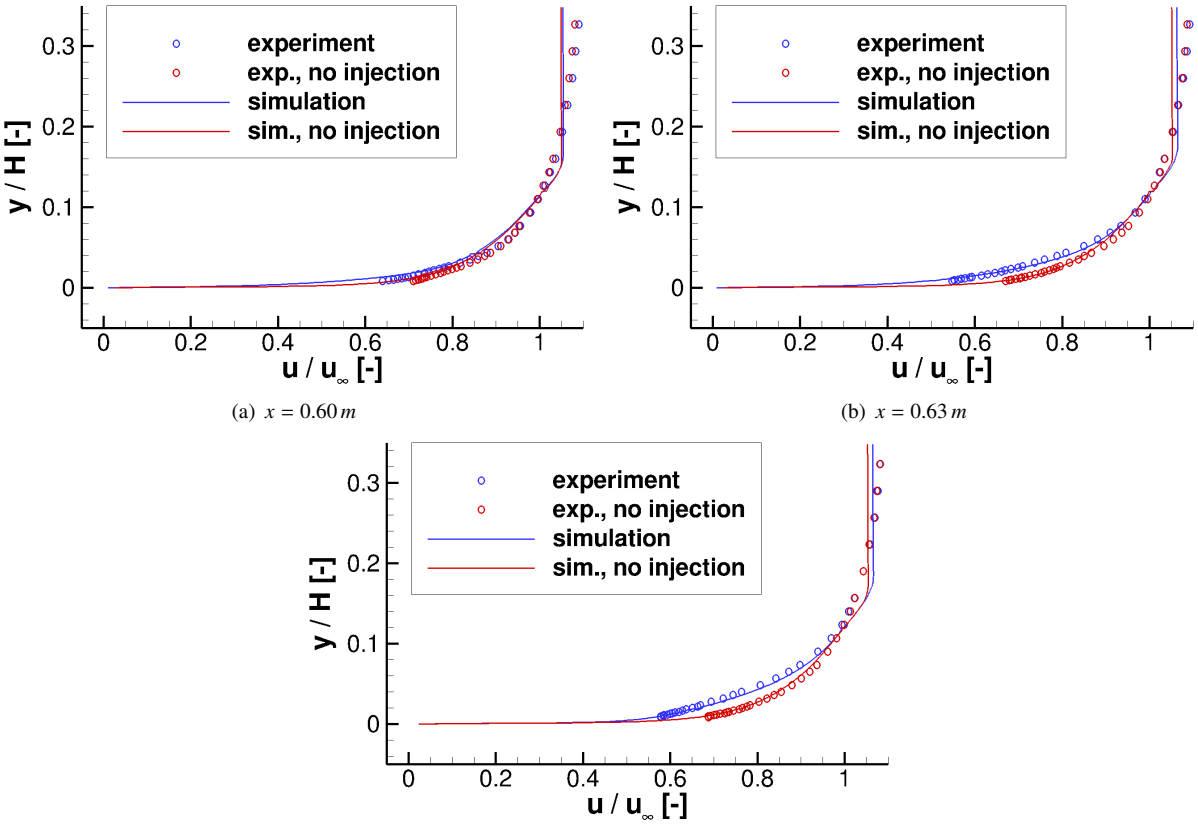

(a) $x = 0.60\,m$

(b) $x = 0.63\,m$

(c) $x = 0.66\,m$

Figure 8: Velocity boundary profiles for the hot gas channel flow.

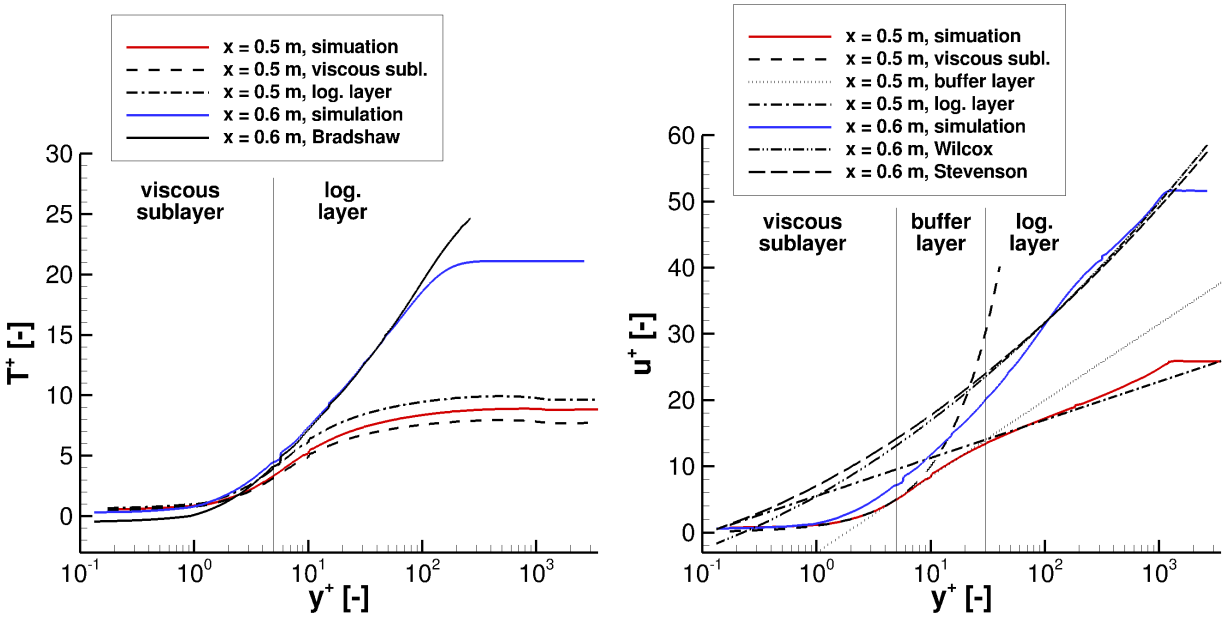

(a) dimensionless temperature T^+

(b) dimensionless velocity u^+

Figure 9: Dimensionless temperature and velocity boundary profiles for the streamwise positions $x = 0.5$ m upstream of the injection and $x = 0.6$ m above the injection.

Table 4: Comparison of simulation results with experimental data [9] for the local skin friction coefficients without and with cooling gas injection.

	$\frac{c_{f,0}}{2}$, no injection		$\frac{c_f}{2}$, with injection		$\frac{c_f}{c_{f,0}}$	
	simulation	experiment	simulation	experiment	sim.	exp.
$x = 0.60\,m$	$1.639 \cdot 10^{-3}$	$1.574 \cdot 10^{-3}$	$0.534 \cdot 10^{-3}$	$0.575 \cdot 10^{-3}$	0.326	0.366
$x = 0.63\,m$	$1.632 \cdot 10^{-3}$	$1.477 \cdot 10^{-3}$	$0.483 \cdot 10^{-3}$	$0.406 \cdot 10^{-3}$	0.296	0.275
$x = 0.66\,m$	$1.624 \cdot 10^{-3}$	$1.496 \cdot 10^{-3}$	$1.398 \cdot 10^{-3}$	-	0.861	-

At the position $x = 0.6\,\mathrm{m}$ above the cooling gas injection, different formulas have to be applied. Hence, we compare the simulation results with the curves computed by

$$T^+ = \frac{u_\tau}{v_w}\left[\left(1 + \frac{u\,v_w}{u_\tau^2}\right)^{Pr_t}\left(1 - 1.1\frac{v_w}{u_\tau} + \left(\frac{v_w}{u_\tau}\right)^2\right) - 1\right] \tag{60}$$

for the temperature originally proposed by Isaacson and AlSaji [25] and revised by Bradshaw [26] and

$$u^+ = 2.5\ln(y^+) + \frac{3.36 + 0.63\ln(y^+)}{0.4}\frac{v_w}{u_\tau}\ln(y^+) + 5.5 \tag{61}$$

for the velocity by Wilcox [20]. Another alternative by Stevenson [27] reads

$$u^+ = \frac{u_\tau}{v_w}\left[\left(\frac{1}{2}\frac{v_w}{u_\tau}\left(2.5\ln(y^+) + 5.5\right) + 1\right)^2 - 1\right]. \tag{62}$$

All three formulas (60) - (62) are based on Prandtl's mixing length theory and were derived by curve fitting to experimental data. The simulation results for the cooled position agree with all three curves in the logarithmic layer for which the formulas are valid only. Note that for larger values of y^+, all above-mentioned formulas are not applicable anymore as can be clearly seen in both plots.

In the analysis of the experiment, the local skin friction coefficient c_f was estimated, for instance, by applying a procedure according to Clauser [28]. Since the computation is related to a logarithmic law of the wall, there is no possibility to estimate c_f in the wake of the injection ($x = 0.66\,\mathrm{m}$) for which no such law exists. The results [9] are listed in Tab. 4 together with the corresponding simulation results. The effect of the cooling gas injection, i.e., the strong reduction of the skin friction, is reproduced by the simulation in a comparable order of magnitude.

6. Conclusion and Outlook

Coupling of porous medium flow to pure fluid flow is a field of research which lacks in both theoretical and numerical investigations. To the authors' knowledge, there has been no other approach of performing a fully coupled simulation of transpiration cooling so far. The weak coupling using boundary conditions performed in this study leads to convergence and reasonable results.

Our numerical investigation of the influence of cooling gas injection on the boundary layer of a subsonic turbulent hot gas channel flow confirms that the implemented two-domain approach is suitable for the simulation of subsonic transpiration cooling. To obtain the stationary equilibrium solution of the coupled problem, the finite volume solver for the hot gas flow and the finite element solver for the porous medium flow are applied alternately. Each of the two solvers can be converged to a steady state with respect to the coupling conditions generated from the current solution of the other solver. The iterative solution process is stopped when in both solvers the maximal absolute difference of a flow quantity of the respective solver at the coupling interface becomes smaller than a given tolerance compared with the previous iteration. The choice of suitable coupling conditions is a complex task since it is still under discussion which flow quantities should remain continuous at the interface. Our approach was validated in [17], but there is still room for improvements, e.g., by taking into account the roughness of the porous surface.

The simulation results are in good agreement with the experimental data, especially bearing in mind possible numerical errors on the simulation side and measurement inaccuracies on the experimental side. In addition, some values of the experimental data cannot be measured directly but have to be computed from other measured quantities (velocity) or by incorporating empirical relations (local skin friction). The numerical investigation also provides complementary insight into the cooling effect on the boundary layer since it is impossible to cover the whole boundary

layer in the experiment. More precisely, in the experiments considered for this paper, the first values above the wall were measured at a height of approximately 25 % of the boundary layer thickness.

Further simulations have to be carried out to confirm the results of this study and to further improve the implemented numerical methods. Therefore, three-dimensional computations and test cases with coolants other than air should be investigated. Additionally, test cases with the porous probe being mounted into the wall such that the carbon fibers are orthogonal instead of parallel to the flow direction would be interesting.

Regarding the turbulence modeling in the hot gas channel flow, an improvement was achieved by taking into account the mass injection into the boundary layer as proposed by the boundary condition (16) of Wilcox's turbulence model. This model also offers a boundary condition for rough walls such that small scale effects induced by the porous medium roughness can be accounted for without resolving the roughness. By combining these two boundary conditions, the model could be further improved. Another approach to include the small scale effects into our model is to employ homogenization techniques to determine effective boundary conditions for the cooling gas injection. For incompressible, laminar flow, results are reported in [29].

A long-term objective is the simulation of transpiration cooling of rocket thrust chambers in which much higher pressures ($> 10\,\mathrm{MPa}$) and temperatures ($> 3500\,\mathrm{K}$) occur than in the test case investigated in this study. For this purpose, our implementation has to be extended to account for the chemical properties of the propellants such as liquid oxygen/liquid hydrogen and the associated chemical processes taking place in the thrust chamber conditions. In addition, it is possible that the flow through the porous material becomes turbulent such that the model for the porous medium flow would have to be modified.

Acknowledgments

Financial support has been provided by the German Research Foundation (Deutsche Forschungsgemeinschaft – DFG) in the framework of the Sonderforschungsbereich Transregio 40.

The authors would like to thank Prof. Dr. J. von Wolfersdorf and S. Schweikert, University of Stuttgart, Dr. T. Langener, European Space Agency, and M. Selzer, DLR Stuttgart, for fruitful discussions on the modeling of porous medium flow as well as on the coupling problem and for providing us with experimental data.

References

[1] Gotzen,T. 2013. Numerical Investigation of Film and Transpiration Cooling. Diss. RWTH Aachen.

[2] Linn,J., Kloker,M.J. 2008. Numerical Investigations of Film Cooling and its Influence on the Hypersonic Boundary-Layer Flow. In: Gülhan, A. (Ed.), *RESPACE - Key Technologies for Reusable Space Systems, NNFM*, 98:151–169, Springer.

[3] Linn, J., Kloker, M. J. 2011. Effects of wall-temperature conditions on effusion cooling in a Mach-2.67 boundary layer. *AIAA J.*, 49(2):299–307.

[4] Linn, J., Keller, M. and Kloker, M. J. 2010. Effects of Inclined Blowing on Effusion Cooling in a Mach-2.67 Boundary Layer. *Annual Report SFB TRR40 2010*, München, 55–67.

[5] Selzer, M., Langener, T., Hald, H. and von Wolfersdorf, J. 2009. Production and Characterization of Porous C/C Material. In: N. A. Adams, R. Radespiel, T. Sattelmayer, W. Schröder, B. Weigand (Eds.), *Annual Report SFB TRR40 2009*, München, 75–85.

[6] Gülhan, A. and Braun, S. 2011. An experimental study on the efficiency of transpiration cooling in laminar and turbulent hypersonic flows. *Exp. Fluids* 50(3):509–525.

[7] Langener, T. 2011. A Contribution to Transpiration Cooling for Aerospace Applications Using CMC Walls. Diss. Univ. Stuttgart.

[8] Langener, T., von Wolfersdorf, J., Selzer, M. and Hald, H. 2012. Experimental investigations of transpiration cooling applied to C/C material. *Intl. J. Thermal Sc.*, 54:70–81.

[9] Schweikert, S., von Wolfersdorf, J., Selzer, M. and Hald, H. 2013. Experimental Investigation on Velocity and Temperature Distributions of Turbulent Cross Flows over Transpiration Cooled C/C Wall Segments. *5th European Conference for Aeronautics and Space Sciences (Eucass), München*.

[10] Bramkamp, F., Lamby, Ph. and Müller, S. 2004. An adaptive multiscale finite volume solver for unsteady and steady state flow computations. *J. Comp. Phys.*, 197(2):460–490.

[11] Bramkamp, F. 2003. Unstructured *h*-Adaptive Finite-Volume Schemes for Compressible Viscous Fluid Flow. Diss. RWTH Aachen.

[12] Müller, S. 2003. Adaptive Multiscale Schemes for Conservation Laws. *Lecture Notes on Computational Science and Engineering*, **27**, 1st edition, Springer.

[13] Lamby, Ph. 2007. Parametric Multi-Block Grid Generation and Application to Adaptive Flow Simulations. Diss. RWTH Aachen.

[14] Wilcox, D. C. 2008. Formulation of the *k*-ω turbulence model revisited. *AIAA J.*, 46(11):2823–2838.

[15] Bangerth, W., Hartmann, R. and Kanschat, G. 2007. deal.II - a general-purpose object-oriented finite element library, *ACM Trans. Math. Softw.*, 33(4):24/1–24/27.

[16] Dahmen, W., Gerber, V., Gotzen, T. and Müller, S. 2013. Numerical Simulation of Effusion Cooling through Porous Media. *5th European Conference for Aeronautics and Space Sciences (Eucass), München*.

[17] Dahmen, W., Gotzen, T., Müller, S. and Rom, M. 2014. Numerical simulation of transpiration cooling through porous material. *Int. J. Numer. Meth. Fluids*,76(6):331–365.

[18] Dahmen, W., Gerber, V., Gotzen, T. and Müller, S., Rom, M. and Windisch, C. 2014. Numerical Simulation of Transpiration Cooling with a Mixture of Thermally Perfect Gases. Submitted to *joint WCCM - ECCM - ECFD 2014 Congress, Barcelona*.

[19] White, F. M. 2009. *Fluid Mechanics*. McGraw-Hill.

[20] Wilcox, D. C. 2006. *Turbulence Modeling for CFD*. DCW Industries Inc., 3rd edition.

[21] Nield, D. A. and Bejan, A. 2006. *Convection in Porous Media*. Springer, 3rd edition.

[22] L'Ecuyer, M. R. and Colladay, R. S. 1972. Influence of porous-wall thermal effectiveness on turbulent-boundary-layer heat transfer. *NASA Technical Note*, D-6837.

[23] Huang, P. G. and Coleman, G. N. 1994. Van Driest transformation and compressible wall-bounded flows. *AIAA J.*, 32(10):2110–2113.

[24] von Kármán, T. 1939. The analogy between fluid friction and heat transfer. *Trans. ASME*, 61:705–710.

[25] Isaacson, J. K. and AlSaji, S. J. 1969. Temperature laws for a turbulent boundary layer with injection and heat transfer. *AIAA J.*, 7(1):157–159.

[26] Bradshaw, P. 1970. Comments on "Temperature laws for a turbulent boundary layer with injection and heat transfer". *AIAA J.*, 8(7):1375–1376.

[27] Stevenson, T. N. 1963. A Law of the Wall for Turbulent Boundary Layers with Suction and Injection. The College of Aeronautics, Cranfield Rep. Aero. No. 166.

[28] Clauser, F. H. 1954. Turbulent boundary layers in adverse pressure gradients. *Journal of the Aeronautical Sciences*, 21(2):91–108.

[29] Jäger, W. and Mikelic, A. 2001. On the roughness-induced effective boundary conditions for a viscous flow. *J. Diff. Eq.* 170:96–122.